

Precision Measurement of the ^{87}Rb Tune-Out Wavelength in the Hyperfine Ground State $F=1$ at 790 nm

Felix Schmidt,^{1,2} Daniel Mayer,^{1,2} Michael Hohmann,¹ Tobias Lausch,¹ Farina Kindermann,¹ and Artur Widera^{1,2}

¹*Department of Physics and Research Center OPTIMAS, University of Kaiserslautern, Germany*

²*Graduate School Materials Science in Mainz, Gottlieb-Daimler-Strasse 47, 67663 Kaiserslautern, Germany*

(Dated: December 14, 2015)

We report on a precision measurement of the D line tune-out wavelength of ^{87}Rb in the hyperfine ground state $|F=1, m_F=0, \pm 1\rangle$ manifold at 790 nm, where the scalar ac Stark shifts of the D_1 and the D_2 lines cancel. This wavelength is sensitive to usually neglected contributions from vector and tensor ac Stark shifts, transitions to higher principle quantum numbers, and core electrons. The ac Stark shift is probed by Kapitza-Dirac scattering of a Rubidium Bose-Einstein condensate in a one-dimensional optical lattice in free space and controlled magnetic environment. The tune-out wavelength of the magnetically insensitive $m_F=0$ state was determined to 790.018 58(23) nm with sub pm accuracy. An *in situ* absolute polarization, and magnetic background field measurement is performed by employing the ac vector Stark shift for the $m_F = \pm 1$ states. Comparing our findings to theory, we get quantitative insight into atomic physics beyond commonly used two-level atom approximations or the neglect of inner shell contributions.

PACS numbers: 32.10.Dk, 37.10.Jk, 32.10.Fn

I. INTRODUCTION

Energy shifts of atomic levels due to light-matter interaction have enabled optical traps for neutral atoms with numerous applications in state-of-the-art quantum technology as well as atomic and molecular physics. Of particular interest are so-called magic wavelengths, where contributions originating from the coupling to different atomic transitions cancel in some quantity. Important examples are the cancellation of differential light shifts in atomic traps for spectroscopic applications and metrology [1–4], the minimization of differential light shifts for different hyperfine states [5, 6], or engineering of state-dependent traps [7–10].

In mixed-species experiments, the usage of magic wavelength dipole traps facilitates engineering of species-selective optical traps, where in a mixture of two ultracold atomic species only one is optically trapped, while the other experiences a zero-crossing of the total energy shift for this so-called tune-out wavelength [11, 12]. Beyond the application of these tune-out wavelengths for quantum engineering, they yield information about the exact atomic level structure. This can be used to compare with *ab-initio* calculations to refine the models of the atom and fundamental atomic data [12]. While there are versatile theoretical studies on tune-out wavelengths in alkali metals [11–17], only few measurements have been performed in Potassium [18, 19], and Rubidium [20, 21], using interferometry and, respectively, light shift cancellation techniques.

In our case, the system is designed to provide a species-selective optical lattice for single $^{133}\text{Cesium}$ (Cs) atoms in a mixture with a $^{87}\text{Rubidium}$ (Rb) Bose-Einstein condensate (BEC) [22]. The tune-out wavelength for Rb at 790 nm results from blue detuning to the D_1 transition at 795 nm and red detuning to the D_2 transition at 780 nm, so the ac Stark shifts cancel.

Here, we report on the measurement of this tune-out wavelength in the ground state manifold $|F=1, m_F=0, \pm 1\rangle$ in the absence of additional light fields and a controlled magnetic environment. Since the dominant scalar ac Stark shifts of both D lines add to zero, our observation reveals usually neglected contributions, such as vector and tensor polarizabilities, transitions to higher quantum numbers, and the influence of core electrons to the scalar polarizability.

We measure the tune-out wavelength of the $m_F=0$ state, where no vector ac Stark shift is present, with an accuracy improvement by a factor of 10 compared to an earlier measurement [23]. We compare our value with a theoretical model, obtained from a recent measurement in a related system [21]. By employing the vector ac Stark shift in the case of $m_F = \pm 1$, *in situ* information about the absolute lattice polarization at a sub-percent level and the magnetic background field is gained.

II. AC STARK SHIFT AND POLARIZABILITY

To reveal the influence of additional contributions to the ac Stark shift, the scalar components from the D lines have to be calculated accurately. Therefore, instead of using common approximations, *i.e.* averaging the transitions' line widths [24] and neglecting the hyperfine structure (HFS) [11], we sum over all dipole allowed hyperfine transitions, coupled by the light field, following the formalism given in [13, 25]. Here, the atom is interacting with an electromagnetic wave

$$\vec{E} = \frac{1}{2} E_0 \vec{e} e^{-i(\omega t - kz)} + \text{c.c.} \quad (1)$$

of amplitude E_0 , frequency ω , and wave number $k = 2\pi/\lambda$, propagating along the z direction, where λ is the laser wavelength. The vector \vec{e} denotes an arbitrary complex

polarization, that is described by a parametric angle θ_0 as

$$\vec{e} = \hat{e}_x \cos \theta_0 + i\hat{e}_y \sin \theta_0, \quad (2)$$

with the degree of circular polarization $A = \sin 2\theta_0$. The total energy shift is then calculated for an atom in the hyperfine Zeeman state $|n(IJ)Fm_F\rangle$, with main quantum number n , nuclear spin I , electronic angular momentum J , total angular momentum F with $\vec{F} = \vec{J} + \vec{I}$, and its projection to the quantization axis m_F . This yields an ac Stark shift of

$$V_{nFm_F}^{(2)}(\lambda) = -\left(\frac{1}{2}E_0\right)^2 \left[\alpha_{nF}^s(\lambda) + C\frac{m_F}{2F}\alpha_{nF}^v(\lambda) - D\frac{3m_F^2 - F(F+1)}{2F(2F-1)}\alpha_{nF}^T(\lambda) \right], \quad (3)$$

with the state and wavelength dependent scalar, vector, and tensor polarizabilities $\alpha_{nF}^s(\lambda)$, $\alpha_{nF}^v(\lambda)$, and $\alpha_{nF}^T(\lambda)$ respectively, summing over all contributions from dipole allowed transitions to excited states $|n'(IJ')F'm'_F\rangle$. The parameters $C = A \cos \theta_k$, and $D = (3 \cos^2 \theta_p - 1)/2$ depend on the light field's polarization. Here, the orientation of the light field with respect to the system's quantization axis along the magnetic field vector \hat{B} is given by the angle θ_k between the quantization axis and the wave vector, and θ_p between the quantization axis and the polarization vector, respectively. By factorizing the dependencies on I , F , m_F , F' , and m'_F , all polarizabilities are reduced to the dipole transition matrix elements $\langle n'J' | e\hat{r} | nJ \rangle$, which can be taken from literature.

Note that only states with $m_F \neq 0$ show a vector ac Stark shift, which depends on the polarization of the light field. Nevertheless, the tensor polarizability, which vanishes for $J = 1/2$ if only fine structure splitting is taken into account [13], shows an ac Stark shift contribution even in the $m_F = 0$ case.

Figure 1 illustrates the wavelength and light polarization dependence of the ac Stark shift. The vector ac Stark shift disappears for $m_F = 0$, but can shift the tune-out wavelengths of the $m_F = \pm 1$ states by up to 2 nm in the case of circularly polarized light ($A = \pm 1$).

III. EXPERIMENTAL METHOD

We measure the ac Stark shift around the tune-out wavelength by employing Kapitza-Dirac (KD) scattering, the diffraction of a matter wave at a light grating. KD scattering has been originally introduced [26] and measured [27, 28] for electrons. The diffraction of neutral atoms was demonstrated for atomic beams [29, 30], ultracold clouds [31], and BECs [32], and since then became a standard tool for atom interferometry applications [33, 34] and optical lattice characterization [35–37]. We perform the KD experiment by flashing a Rb BEC for a duration $\tau = 12 \mu\text{s}$ with a one-dimensional static optical lattice, derived from two counterpropagating beams

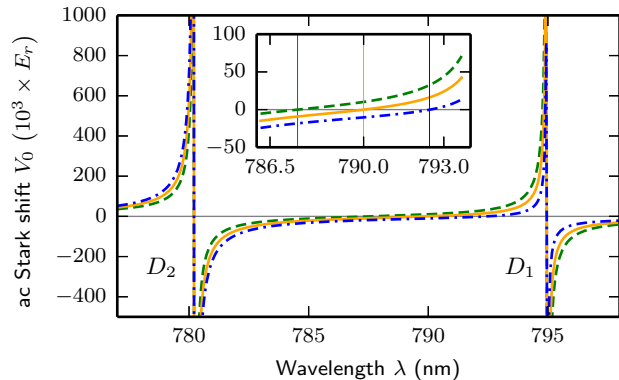


FIG. 1. The ac Stark shift V_0 for Rb atoms in the $m_F = 0$ (solid), $m_F = +1$ (dashed), and $m_F = -1$ (dashed-dotted) ground states $|F = 1\rangle$, for right handed (σ^+) polarized light ($\theta_0 = \pi/4$). V_0 is given in multiples of the photon recoil E_r at 790 nm, and a typical light intensity in our experiment of $I = 136 \text{ mW/cm}^2$. The inset shows a magnified view of the tune-out wavelengths for the three m_F states (vertical lines). The tune-out wavelengths of the $m_F = \pm 1$ states are shifted by more than 2 nm with respect to the $m_F = 0$ states due to the vector ac Stark shift.

along z , with wavelength λ and linear polarization parallel to x . The earlier discussed ac Stark shift results in a lattice potential of V_0 . The Rb matter wave scatters at the light grating of periodicity $\lambda/2$, imposing a momentum transfer of multiples of $2\hbar k = 2\pi\hbar\frac{2}{\lambda}$, with $\hbar = h/2\pi$ and Planck's constant h . In the theoretical description, the particle motion during the interaction is neglected (Raman-Nath regime) [30, 38], yielding an occupation of the momentum states $p = 2N\hbar k$ ($N = 0, \pm 1, \pm 2, \dots$) with a respective probability of

$$P_N(V_0, \tau) = J_N^2\left(\frac{V_0\tau}{2}\right), \quad (4)$$

where $J_N(\theta)$ are the Bessel functions of the first kind. In our system, the Raman-Nath condition is fulfilled for absolute lattice depths $|V_0| \ll 125 E_r$, given in multiples of the photon recoil $E_r = (\hbar k)^2/2m_{\text{Rb}}$, with Rb mass m_{Rb} .

Experimentally, both lattice beams are derived from a single-frequency Titanium Sapphire (Ti:Sa) laser and intensity-modulated with acousto-optic modulators (AOM) in each lattice arm, yielding a power of up to 450 mW per beam at a waist of 29 μm . The AOMs shift the laser frequency by $-160 \text{ MHz} \pm 1 \text{ Hz}$ and therefore the wavelength by $\Delta\lambda = +0.42 \text{ pm}$ (at $\lambda = 790 \text{ nm}$). The radio frequency source, driving both AOMs is switched by means of a voltage controlled attenuator (VCA), limiting the pulse edges to a $1/e$ -time of 1.7 μs . In a crossed dipole trap at $\lambda = 1064 \text{ nm}$ a BEC of typically 2.5×10^4 atoms is prepared. The BEC is optically pumped to the absolute ground state $|F = 1, m_F = +1\rangle$ and driven into

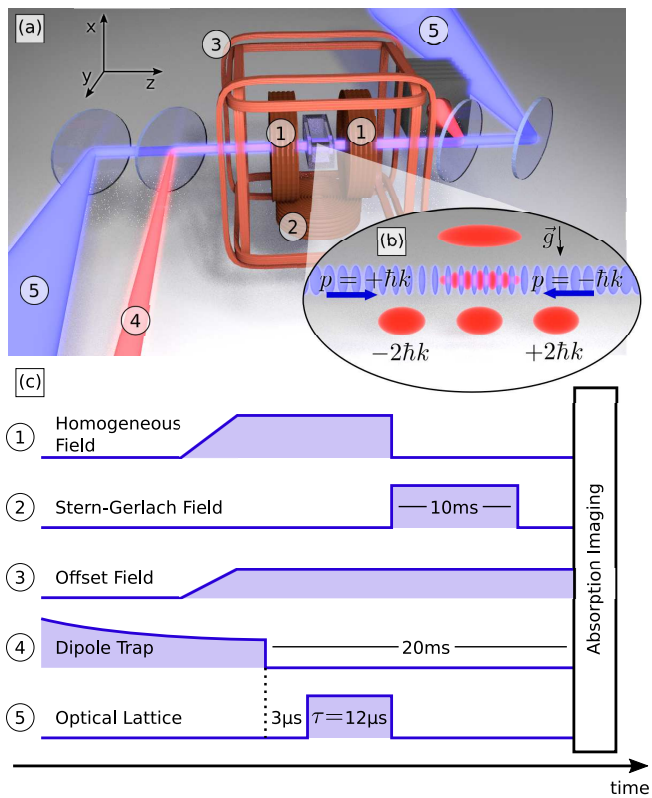


FIG. 2. Experimental Setup. (a) Simplified artist's view on the experiment. The coil setup used for magnetic field control consists of the homogeneous field coils (1), the Stern-Gerlach coil (2), and 3D compensation coils (3). The dipole trap beam (4) and the two counterpropagating lattice beams (5) are overlapped by dichroic mirrors on the main axis through the glass cell. (b) Schematic scattering process. When applying the lattice pulse on the free falling BEC, atoms are scattered into higher momentum orders $\pm 2N\hbar k$ depending on the potential depth. (c) Schematic time line for the experimental sequence. After preparing the BEC in the dipole trap and setting the magnetic field to the desired value, the dipole trap is switched off and after a delay of $3\mu\text{s}$, the lattice pulse of $\tau = 12\mu\text{s}$ duration is applied. Subsequently, the Stern-Gerlach field gradient is switched on and after 20 ms the atoms are imaged via absorption imaging along the y -axis.

a desired m_F state by means of a radio frequency transition. Details on our BEC preparation scheme are given in [22].

Although KD scattering experiments have also been performed in thermal gases [31], the BEC system features a lower thermal momentum spread. In particular, the thermal spread is smaller than the momentum transfer of multiples of $2\hbar k$, which allows for separating and counting populations of higher momentum orders with standard time of flight (TOF) absorption imaging.

Figure 2 shows our setup and a typical experimental sequence. The KD pulse is applied $3\mu\text{s}$ after releasing the BEC from the optical dipole trap, so we exclude any influence of the trap [39] on the measured tune-out wave-

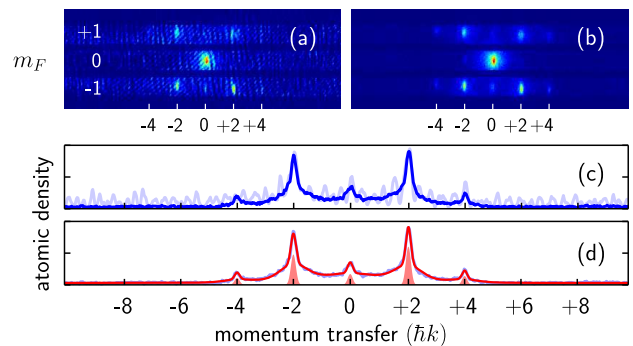


FIG. 3. KD image for a Rb spin mixture. (a) KD scattering image for $12\mu\text{s}$ pulse at a lattice wavelength of 790.018 nm after 20 ms TOF. The m_F states are distinguished by applying a magnetic Stern-Gerlach field along the gravitation axis x . The wavelength corresponds to the tune-out wavelength of the $m_F = 0$ state. $m_F = +1$ and $m_F = -1$ show scattering into higher momentum orders due to the vector ac Stark shift. (b) The use of an improved absorption image calculation suppresses interference fringes of the imaging laser and background noise, increasing the SNR from 34 to 95. (c) The signal is vertically binned in the highlighted areas for each m_F state. The improved image calculation (solid line) is compared to the standard technique (shaded). (d) A multi-Gaussian (solid line) is fitted to the line data (shaded line) from (b). The transfers are determined from the areas of the BEC peaks (shaded area). The population of the $\pm 4\hbar k$ peaks correspond to less than 1750 Rb atoms each.

length. During the KD pulse, three orthogonal pairs of offset field coils create a magnetic field of up to 3 G in each direction. Additional homogeneous field coils allow to apply a strong offset field along z of up to several 100 G. Due to the VCA's switching response and fluctuations of the optical setup, the lattice pulse shape deviates from an ideal square wave. Analyzing the time dependent intensity of both lattice beams, we obtain a reduction of the effective pulse duration from ideally $12\mu\text{s}$ to $8.75\mu\text{s}$ with respect to the maximum lattice intensity, and an intensity fluctuation of 2.3% rms, respectively. The latter results in a reduction of the lattice potential V_0 on the same order of magnitude. Note that the fluctuation of V_0 does not affect the zero-crossing point of the lattice potential.

Figure 3 shows a KD measurement of a Rb spin mixture after 20 ms TOF. The magnetic states $m_F = 0, \pm 1$ are spatially separated by applying an inhomogeneous magnetic Stern-Gerlach field after the KD flash.

The population of each $2N\hbar k$ momentum state is fitted with a double Gaussian, representing a superposition of a thermal background and a BEC peak. Since the thermal contributions cannot be well distinguished from each other, only the BEC contributions are included into the analysis according to equation (4). Note that the scattering amplitudes $P_N(V_0, \tau)$ are equal for positive and negative lattice potentials, and therefore give a measure

of the absolute ac Stark shift. Therefore, the sign has to be determined from the theoretical model.

When measuring KD at weak lattice potentials V_0 , the atomic density signal in higher momentum states approaches the detection threshold of our imaging system, which is mainly determined by the occurrence of fringes in the absorption images. Since the atomic density is calculated as $\propto -\log(S_i/R_i)$ from the actual absorption image S_i containing the shadow of the BEC, and a reference image R_i with only the probe laser light, any fluctuation of interference patterns between the two images results in fringes in the atomic density (see figure 3(a)).

This effect is strongly suppressed by using an optimum reference image R_{best} , that reproduces the background properties of the signal shot S_i [40], and thereby the specific interference pattern. We compute R_{best} as a linear combination $\sum_k^M c_k R_k$ of up to 500 reference images from a base $[R_k]$, so it optimally matches a signal-free area in the absorption signal S_i with a size of roughly 200×300 pixel. The least square fitting algorithm, given in [40] was optimized by diagonalizing the base of reference images $[R_k]$, allowing for a computation time of less than 100 ms per absorption image on a standard personal computer. The approach avoids fringes, created by time varying interference patterns of the probe laser beam at the best and even yields a reduction of photon shot noise [40], increasing the signal to noise ratio (SNR) by a factor of at least 3 in our measurements.

IV. RESULTS

A. $m_F = 0$ State Measurement

We measure the tune-out wavelength of the $m_F = 0$ state, where the scalar and the tensor, but no vector ac Stark shift is present. The laser wavelength is measured with a wavelength meter, offering a resolution of 50 MHz, and an automatic calibration to a built-in wavelength standard. We have validated the calibration by measuring the wavelength of a laser, stabilized to the Rb $|5S_{1/2} F = 1\rangle \rightarrow |5P_{3/2} F = 2\rangle$ transition [41], with an absolute accuracy of 20 MHz. For the measurements we use a magnetic offset field of $(B_{x_0}, B_{y_0}, B_{z_0}) = (0.4, 0.3, -0.7)$ G and apply a homogeneous quantization field B_z along z . Since for $m_F = 0$ the nonlinear Zeeman energy is negligible for weak magnetic fields, we do not expect a magnetic field dependence of the tune-out wavelength. However, the measurement is limited to $B_z \approx 100$ G. For higher fields, an asymmetric background in the absorption images occurs, which perturbs the momentum transfer fits. We attribute the asymmetric background to a superposition of the homogeneous quantization field and the Stern-Gerlach field.

Figure 4 shows the measurement of the lattice potential depth around the tune-out wavelength for various offset fields B_z in a range of 5 G to 100 G. The dependence of the potential $V_0(\lambda)$, taken from equation (3) is approxi-

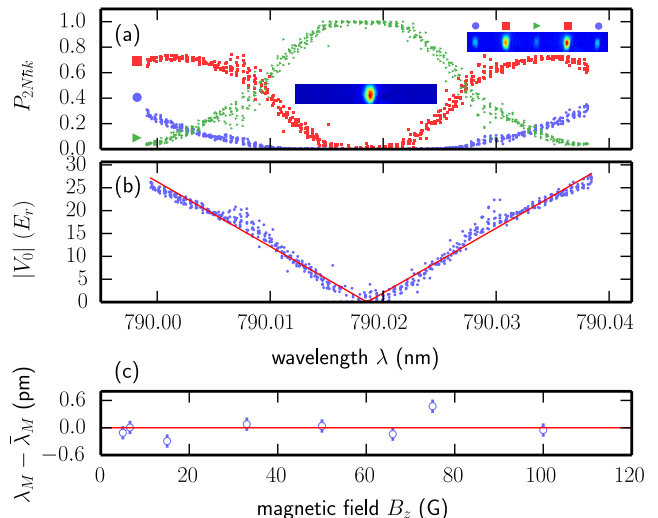


FIG. 4. Tune-out wavelength measurement of Rb in the $|F = 1, m_F = 0\rangle$ state. (a) From the KD scattering images, the populations in the zero momentum state (triangle), $\pm 2\hbar k$ (square), and $\pm 4\hbar k$ (circle) state were extracted. Insets show samples of KD images for vanishing (center) and maximal potential (right). (b) The resulting lattice potential V_0 (dots) was fitted with the model of eq. (5) with the tune-out wavelength λ_M (solid line). (c) For various magnetic offset fields B_z the tune-out wavelength has been measured. The values scatter around the average of $\bar{\lambda}_M = 790.018\,58$ nm (solid line). The error bars are calculated from the fitting uncertainties of (b) and the wavelength measurement calibration.

mately linear with a maximum deviation of 0.25% in the measured wavelength range, and writes

$$V_0(\lambda) = \frac{\partial V_0}{\partial \lambda}(\lambda - \lambda_M), \quad (5)$$

with the slope $\frac{\partial V_0}{\partial \lambda}$, and the tune-out wavelength λ_M . Since the KD scattering analysis yields absolute values, $|V_0(\lambda)|$ is fitted to the potentials. We average the λ_M data and obtain a tune-out wavelength of $\bar{\lambda}_M = 790.018\,58(23)$ nm for the $|F = 1, m_F = 0\rangle$ state, providing a 10-fold accuracy improvement compared to the previous measurement of 790.018(2) nm in the same internal state [23]. We compare our result to the model from equation (3), assuming a scalar polarizability of

$$\alpha_{n,JF}^s(\lambda) = \alpha_F^{5s-5p}(\lambda) + \alpha_J^{5s-6p+} + \alpha^{c, cv}. \quad (6)$$

Here, $\alpha_F^{5s-5p}(\lambda)$ contains all wavelength dependent scalar polarizabilities from the Rb D lines, that we calculate from the dipole allowed hyperfine transitions with respective energy splitting [25]. Transitions to higher P states are represented by α_J^{5s-6p+} , where only the fine structure is taken into account. The contribution of core electrons and core electron - valence electron interaction is represented by $\alpha^{c, cv}$ [12]. For α_J^{5s-6p+} as well as $\alpha^{c, cv}$

TABLE I. Comparison of the measured tune-out wavelength $\lambda_{M,\text{experiment}}$ of the Rb $|F=1, m_F=0\rangle$ state with a theoretical model. First, the tune-out wavelength $\lambda_{M,5s-5p, \text{theo}}$ is calculated from the wavelength dependent D polarizability. We compare predictions, using the reduced dipole matrix elements from direct measurement (a) from [41], and the more accurate reduced dipole moment $d_{3/2}$ from [41], and the ratio $R = |d_{3/2}|^2/|d_{1/2}|^2$ from [21] (b), respectively. A more accurate model $\lambda_{M,\text{total, theo}}$ is obtained, when further polarizability contributions are included. Each shifts the tune-out wavelength by $\Delta\lambda_{\text{tensor}}$ (tensor) $\Delta\lambda_{5s-6p+}$, (transitions to higher quantum numbers), and $\Delta\lambda_{c, cv}$ (core electrons, core-valence electron interaction). Polarizabilities of the latter two components are taken from [21].

matrix elements	$\lambda_{M,5s-5p, \text{theo}}$ (nm)	+ $\Delta\lambda_{\text{tensor}}$ (pm)	+ $\Delta\lambda_{5s-6p+}$ (pm)	+ $\Delta\lambda_{c, cv}$ (pm)	=	$\lambda_{M,\text{total, theo}}$ (nm)	$\lambda_{M,\text{experiment}}$ (nm)
$d_{1/2}, d_{3/2}^{(a)}$	790.0181(56)	0.091(1)	1.203(48)	3.455(38)		790.0228(57)	790.01858(23)
$R, d_{3/2}^{(b)}$	790.01374(1)					790.01850(9)	

most recent values from [21] are used. Since α_J^{5s-6p+} and $\alpha^{c, cv}$ are 4 orders of magnitude smaller than α_F^{5s-5p} , their contribution is negligible in applications using far-off resonance dipole traps. In contrast, at the tune-out wavelength studied here, the polarizabilities of both Rb D lines cancel, revealing these usually negligible components.

Table I compares the theoretical prediction of the tune-out wavelength with our measurement. We first calculate a theoretical value for the tune-out wavelength $\lambda_{M,5s-5p}$, if only the D line contributions α_F^{5s-5p} were present. Each further contribution, *i.e.* the tensor polarizability, the higher transitions, and the core electrons leads to a correction of the tune-out wavelength toward higher wavelengths of in total $\Delta\lambda_M = 4.749(87)$ pm.

Using direct measurements of the reduced dipole matrix elements $d_{1/2} = \langle 5S_{1/2} | d | 5P_{1/2} \rangle$, and $d_{3/2} = \langle 5S_{1/2} | d | 5P_{3/2} \rangle$ in the calculation of the D line contributions from [41] yields an expected tune-out wavelength of 790.0228(57) nm. Here, the uncertainty of 5.7 pm in the prediction does not allow for verifying the expected tune-out wavelength shift of $\Delta\lambda_M = 4.749(87)$ pm. For comparison, we take the more accurately measured ratio of both dipole matrix elements $R = |d_{3/2}|^2/|d_{1/2}|^2$ from [21], that has been gained from determining the tune-out wavelength of the $|F=2, m_F=2\rangle$ state, and get 790.01850(9) nm. Our measurement is in agreement with the model within the 1σ uncertainties, confirming the non-negligible influence of higher transitions and the core-electron polarizability.

We emphasize that in the absence of the vector ac Stark shift for $m_F=0$, the apparent discrepancy with the tune-out wavelength value, obtained for Rb in $|F=2\rangle$ of 790.0324 nm [21] results from different couplings to excited states rather than light polarization or magnetic field effects.

B. $m_F = \pm 1$ State Measurement

Complementary information about the influence of the vector ac Stark shift is gained by investigating the lattice potential of $m_F = \pm 1$. The vector polarizability

$\alpha_F^v(\lambda)$ is constant to the sub-percent level in the measured wavelength range, so the tune-out wavelengths for the $m_F = \pm 1$ states strongly depend on the polarization properties A and θ_k of the light field.

The resulting vector light shift $V_0 \propto A \cos \theta_k m_F \alpha_F^v$ yields a symmetric shift of the tune-out wavelengths with respect to $m_F=0$ according to the sign of the respective m_F state. We perform the measurement analogously to $m_F=0$ for a quantization field of $B_z = 50$ G, parallel to the \hat{k} vector with an angle of $\theta_k = 0.0(1)^\circ$. Therefore, the system is maximally sensitive to the degree of circular lattice polarization A . Figure 5 shows the fitted lattice potentials for both states. The wavelength of minimal remaining lattice potential of $m_F = -1(+1)$ is shifted to a lower (higher) wavelength, indicating a small contribution of left hand circularly polarized (σ^-) lattice polarization. In addition, the lattice potential does not drop to zero as expected. We model this by a fluctuating degree of circular polarization during the KD pulse, effectively

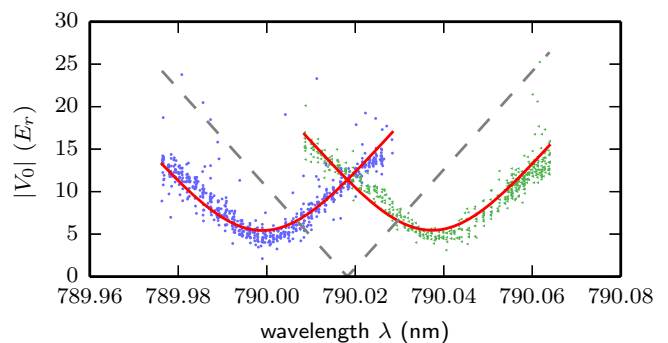


FIG. 5. Lattice potential for the $m_F = \pm 1$ states. Due to the vector Stark shift, the tune-out wavelength for the $m_F = -1$ state (circles, left) is shifted to a lower, and $m_F = +1$ (triangles, right) is shifted to a higher wavelength. As a reference, the $m_F = 0$ (dashed, center) potential is given. The solid line shows one single fit to both the $m_F = +1$ and the $m_F = -1$ state with our model, including a circular degree of polarization A of the lattice (see eq. (7)).

shaking the v -shape potential curve along the λ axis and therefore smoothing out the minimum of the lattice potential. We assume a normally distributed probability of A with a standard deviation of σ_A around the expectation value A_0 . This model yields an effective potential for Rb atoms of

$$|V_0| = \frac{E_0^2}{4} \left[\sqrt{\frac{8\sigma_A^2}{\pi}} e^{-\frac{\gamma^2}{8\sigma_A^2}} + \gamma \operatorname{erf}\left(\frac{\gamma}{\sqrt{8\sigma_A^2}}\right) \right]. \quad (7)$$

Here, $\gamma = \alpha^{s,t} + A_0 \frac{m_F}{F} \alpha^v$ is the lattice potential in the absence of fluctuations in A ($\sigma_A = 0$). We fit the model to the measured $m_F = \pm 1$ data, including the knowledge about the value of the magic wavelength λ_M from the $m_F = 0$ measurement, and using $\partial V_0 / \partial \lambda$, A_0 and σ_A as only free parameters. We obtain $A_0 = -7.80(4) \times 10^{-3}$, which corresponds to an angle of circular polarization of $\theta_0 = -0.223(1)^\circ$, and a fluctuation of $\sigma_A = 4.78(9) \times 10^{-3}$ and $\sigma_{\theta_0} = 0.137(8)^\circ$, respectively. In our setup both lattice arms are linearized before entering the vacuum chamber by a combination of a polarizing beam splitting cube (PBC), a polarization maintaining optical fiber, a half-wave plate, and another PBC. Therefore, we attribute the admixture of circular polarization components to the birefringence of the vacuum chamber windows [42–44], which however does not explain the comparably large and high-frequency fluctuations.

The results from the $m_F = \pm 1$ measurements are of major importance for a possible application of the lattice for species-selective experiments, since even for $A_0 = 0$ and the magnetic field orientation chosen here, the fluctuations lead to a non-vanishing lattice potential for $m_F = \pm 1$ of more than $5 E_r$. For comparison, in the $m_F = 0$ state the residual lattice potential dropped to $1.1 E_r$, when averaging in a wavelength range of ± 1 pm around the tune-out wavelength.

C. Magnetic Field Dependence

After studying the dependence of the vector ac Stark shift on the light polarization, we investigate the influence of the magnetic field orientation on the lattice potential. The vector Stark shift is proportional to the projection $\cos \theta_k = \vec{k} \cdot \vec{B}_t / (|\vec{k}| |\vec{B}_t|)$ of the lattice \vec{k} vector to the total magnetic field \vec{B}_t . We superpose the magnetic background \vec{B}_0 with a known offset field $\vec{B} = (B_x, B_y, B_z)$, and thereby vary \vec{B}_t . With \vec{k} aligned parallel to the z axis, the projection writes

$$\cos \theta_k = \frac{B_{z,t}}{\sqrt{B_{x,t}^2 + B_{y,t}^2 + B_{z,t}^2}} \quad (8)$$

with the spatial components of the total magnetic field $B_{i,t} = B_{0,i} + B_i$ in each direction i . Important cases are $B_z = -B_{0,z}$, where the projection is vanishing as well

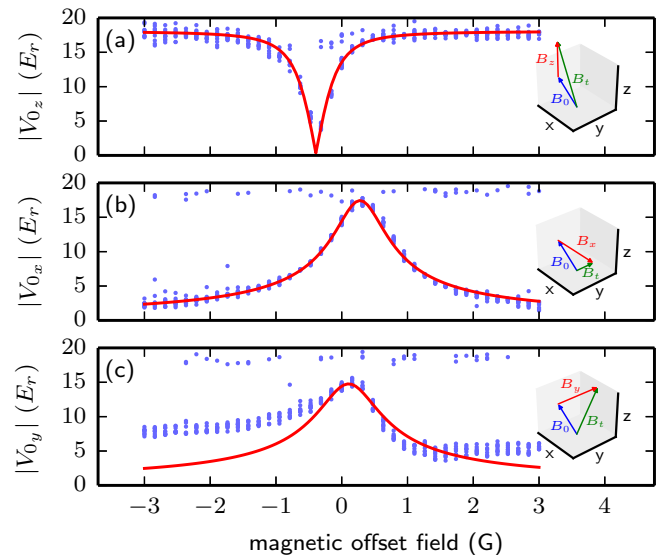


FIG. 6. Measurement of the vector Stark shift. (a) An offset field B_z along the z axis, parallel to the lattice \vec{k} vector is applied. For $B_z = -B_{0,z}$, the quantization axis along the total magnetic field \vec{B}_t is perpendicular to \vec{k} , minimizing the vector light shift. The minimum at $B_{0,z}$ is fitted (solid line) according to our model (eq. 8). (b) For an offset field B_x along the x axis, the projection of \vec{B}_t is maximized for $B_x = -B_{0,x}$. Using $B_{0,z}$ from (a), we get $B_{0,x}$ and $B_{0,y}$ from the fit (solid line). (c) Applying an offset B_y along the y axis, the vector Stark shift is maximized for $B_y = -B_{0,y}$ as well. The solid line shows the model with fit results from (a) and (b). The lattice wavelength was held constant at the tune-out wavelength $790.0182(2)$ nm for all measurements. For each magnetic field, roughly 20 data points were taken.

as $B_x = -B_{0,x}$ and $B_y = -B_{0,y}$, where $\cos \theta_k$ is maximized. We measure the vector ac Stark shift for varying offset along one direction, while keeping the fields in both remaining directions at zero. The lattice wavelength is set to the tune-out wavelength of $m_F = 0$, allowing for maximum sensitivity to the vector ac Stark shift.

Figure 6 shows the measured lattice potential for Rb in the $m_F = +1$ state. From the B_z , and the B_x variation measurement, we obtain a background field of $\vec{B}_0 = (0.28, 0.11, -0.39)$ G. For comparison, using a Hall probe, we measure a magnetic background field of $\vec{B}_{0,H} = (0.25(1), 0.11(1), -0.20(3))$ G in the lab. While $B_{0,x}$, and $B_{0,y}$ agree fairly well with the independent measurement, a discrepancy in $B_{0,z}$ occurs, which we attribute to an additional magnetic background from our setup due to a residual field from the homogeneous field coils. Using the fitted background field, the lattice potential maximum in the B_y variation is reproduced. We suspect the asymmetric wavelength to result from an unwanted magnetic field component of the B_y coils along the z direction. To increase the accuracy of the back-

ground field measurement, optical magnetometry [45] or magnetic field imaging [46] techniques could be applied.

Combining our results of the lattice polarization measurement and the magnetic background field \vec{B}_0 , we gained a valuable understanding of the factors A and $\cos\theta_k$, that determine the influence of the vector Stark shift on the lattice potential *in situ*. In particular, by applying a strong offset field along the x axis, we can reduce the influence of the polarization fluctuations, reaching equally vanishing trapping potentials for all $m_F = 0, \pm 1$ states at the tune-out wavelength, as indicated in the measurement, shown in figure 6 (b).

V. CONCLUSIONS

We have presented an experiment to measure the ac Stark shift around the tune-out wavelength of Rb in the hyperfine ground state manifold $|F = 1, m_F = 0, \pm 1\rangle$ at 790 nm. At the tune-out wavelength, ac Stark shifts from higher transitions and core electrons, as well as vector and tensor polarizabilities are resolved, that are orders of magnitude smaller than the dominant scalar polarizabilities from the D_1 and D_2 line. In addition, by separating the magnetic $m_F = 0, \pm 1$ Zeeman states, we exclude the influence of the vector ac Stark shift on demand. Our measurements feature a Kapitza-Dirac scattering technique, combined with an improved absorption image processing, the absence of additional trapping light fields, and a magnetically controlled environment.

When measuring the $m_F = 0$ state, we exclude the influence of the vector ac Stark shift on the tune-out wavelength. Our value of 790.018 58(23) nm provides a 10-fold accuracy improvement compared to the previous measurement [23] in the same atomic state, and therefore allows for resolving the influence of transitions to higher principle quantum numbers, core electron and core-valence electron contributions to the scalar polarizability α^s of Rb. This confirms a recent measurement of these contributions [21] in a complementary system.

The vector ac Stark shift is included into the system when measuring the lattice potential of the $m_F = -1$ and $m_F = +1$ states. From the shift of the tune-out wavelength with respect to $m_F = 0$, we evaluate the degree of circular polarization $A_0 = -7.80(4) \times 10^{-3}$ of the optical lattice, and its fluctuation $\sigma_A = 4.78(9) \times 10^{-3}$ *in situ*. In addition, by exploiting the dependence of the vector light shift on the quantization field orientation, we have determined the magnetic background field.

Besides probing the atomic level structure beyond common approximations, we apply the tune-out wavelength in our Cs-Rb mixed-species experiment. For our species-selective trapping application, we reach a trap potential selectivity V_{Cs}/V_{Rb} exceeding 1.8×10^3 for the $m_F = \pm 1$ states and more than 3.3×10^3 in the case of $m_F = 0$. In a lattice physics scenario with lattice depth for Cs in the order of $25 E_{r,Cs}$ [47], for Rb this would cause a remaining trap potential of $9.1 \times 10^{-3} E_r$, and a photon scattering rate of 5.7 Hz, where $E_{r,Cs} = (\hbar k)^2/2m_{Cs}$ is the recoil energy for Cs. The species-selective lattice will allow for the study of non-equilibrium interaction effects, such as polaron transport [48], coherence properties of Cs in the Rb bath [49], and Bloch oscillations [50]. Moreover, a full understanding of all relevant ac Stark shift contributions to the Rb potential enables us to engineer m_F state-dependent trapping schemes with variable selectivity and tunable species overlap.

VI. ACKNOWLEDGMENTS

The project was financially supported partially by the European Union via the ERC Starting Grant 278208 and partially by the DFG via SFB/TR49. D.M. is a recipient of a DFG-fellowship through the Excellence Initiative by the Graduate School Materials Science in Mainz (GSC 266), F.S. acknowledges funding by Studienstiftung des deutschen Volkes, and T.L. acknowledges funding from Carl-Zeiss Stiftung.

-
- [1] Z. W. Barber, J. E. Stalnaker, N. D. Lemke, N. Poli, C. W. Oates, T. M. Fortier, S. A. Diddams, L. Hollberg, C. W. Hoyt, A. V. Taichenachev, and V. I. Yudin, *Phys. Rev. Lett.* **100**, 6 (2008).
 - [2] T. Akatsuka, M. Takamoto, and H. Katori, *Nature Physics* **4**, 954 (2008).
 - [3] H. Katori, *Nature Photonics* **5**, 203 (2011).
 - [4] I. Ushijima, M. Takamoto, M. Das, T. Ohkubo, and H. Katori, *Nature Photonics* **9**, 185 (2015).
 - [5] A. D. Ludlow, T. Zelevinsky, G. K. Campbell, S. Blatt, M. M. Boyd, M. H. G. de Miranda, M. J. Martin, J. W. Thomsen, S. M. Foreman, J. Ye, T. M. Fortier, J. E. Stalnaker, S. a. Diddams, Y. Le Coq, Z. W. Barber, N. Poli, N. D. Lemke, K. M. Beck, and C. W. Oates, *Science* **319**, 1805 (2008).
 - [6] N. Lemke, A. Ludlow, Z. Barber, T. Fortier, S. Diddams, Y. Jiang, S. Jefferts, T. Heavner, T. Parker, and C. Oates, *Phys. Rev. Lett.* **103**, 063001 (2009).
 - [7] M. Karski, L. Förster, J. Choi, A. Steffen, W. Alt, D. Meschede, and A. Widera, *Science* **325**, 174 (2009).
 - [8] P. Soltan-Panahi, J. Struck, P. Hauke, A. Bick, W. Plenkers, G. Meineke, C. Becker, P. Windpassinger, M. Lewenstein, and K. Sengstock, *Nature Physics* **7**, 434 (2011).
 - [9] K. Jiménez-García, L. J. Leblanc, R. A. Williams, M. C. Beeler, A. R. Perry, and I. B. Spielman, *Phys. Rev. Lett.* **108**, 1 (2012).
 - [10] N. Belmechri, L. Förster, W. Alt, A. Widera, D. Meschede, and A. Alberti, *J. Phys. B* **46**, 104006 (2013).

- [11] L. J. Leblanc and J. H. Thywissen, *Phys. Rev. A* **75**, 26 (2007).
- [12] B. Arora, M. S. Safronova, and C. W. Clark, *Phys. Rev. A* **84**, 1 (2011).
- [13] P. Rosenbusch, S. Ghezali, V. A. Dzuba, V. V. Flambaum, K. Beloy, and A. Derevianko, *Phys. Rev. A* **79**, 1 (2009).
- [14] M. S. Safronova, U. I. Safronova, and C. W. Clark, *Phys. Rev. A* **86**, 042505 (2012).
- [15] B. Arora and B. K. Sahoo, *Phys. Rev. A* **86**, 033416 (2012).
- [16] J. Jiang, L.-Y. Tang, and J. Mitroy, *Phys. Rev. A* **87**, 032518 (2013).
- [17] J. Jiang and J. Mitroy, *Phys. Rev. A* **88**, 032505 (2013).
- [18] W. F. Holmgren, R. Trubko, I. Hromada, and A. D. Cronin, *Phys. Rev. Lett.* **109**, 1 (2012).
- [19] R. Trubko, J. Greenberg, M. T. S. Germaine, M. D. Gregoire, W. F. Holmgren, I. Hromada, and A. D. Cronin, *Phys. Rev. Lett.* **114**, 1 (2015).
- [20] C. D. Herold, V. D. Vaidya, X. Li, S. L. Rolston, J. V. Porto, and M. S. Safronova, *Phys. Rev. Lett.* **109**, 1 (2012).
- [21] R. H. Leonard, A. J. Fallon, C. A. Sackett, and M. S. Safronova, *Phys. Rev. A* **92**, 52501 (2015).
- [22] M. Hohmann, F. Kindermann, B. Gänger, T. Lausch, D. Mayer, F. Schmidt, and A. Widera, *EPJ Quantum Technology* **2**, 23 (2015).
- [23] G. Lamporesi, J. Catani, G. Barontini, Y. Nishida, M. Inguscio, and F. Minardi, *Phys. Rev. Lett.* **104**, 153202 (2010).
- [24] R. Grimm, M. Weidemüller, and Y. B. Ovchinnikov, *Advances In Atomic, Molecular, and Optical Physics*, Vol. 42 (Academic Press, 2000) pp. 95–170.
- [25] F. Le Kien, P. Schneeweiss, and A. Rauschenbeutel, *The European Physical Journal D* **67**, 92 (2013).
- [26] P. L. Kapitza and P. a. M. Dirac, *Math. Proc. of the Cambridge Phil. Soc.* **29**, 297 (1933).
- [27] P. H. Bucksbaum, D. W. Schumacher, and M. Bashkansky, *Phys. Rev. Lett.* **61**, 1182 (1988).
- [28] D. L. Freimund, K. Aflatooni, and H. Batelaan, *Nature* **413**, 142 (2001).
- [29] E. Arimondo, H. Lew, and T. Oka, *Phys. Rev. Lett.* **43**, 753 (1979).
- [30] P. L. Gould, G. A. Ruff, and D. E. Pritchard, *Phys. Rev. Lett.* **56**, 827 (1986).
- [31] S. Cahn, A. Kumarakrishnan, U. Shim, T. Sleator, P. Berman, and B. Dubetsky, *Phys. Rev. Lett.* **79**, 784 (1997).
- [32] Y. B. Ovchinnikov, J. H. Müller, M. R. Doery, E. J. D. Vredenbregt, K. Helmerson, S. L. Rolston, and W. D. Phillips, *Phys. Rev. Lett.* **83**, 284 (1999).
- [33] R. Sapiro, R. Zhang, and G. Raithel, *Phys. Rev. A* **79**, 043630 (2009).
- [34] W. Li, T. He, and A. Smerzi, *Phys. Rev. Lett.* **113**, 023003 (2014).
- [35] G.-B. Jo, J. Guzman, C. K. Thomas, P. Houser, A. Vishwanath, and D. M. Stamper-Kurn, *Phys. Rev. Lett.* **108**, 045305 (2012).
- [36] P. Windpassinger and K. Sengstock, *Reports on Progress in Physics* **76**, 086401 (2013).
- [37] P. Cheiney, C. M. Fabre, F. Vermersch, G. L. Gattobigio, R. Mathevet, T. Lahaye, and D. Guéry-Odelin, *Phys. Rev. A* **87**, 013623 (2013).
- [38] A. P. Kazantsev, G. I. Surdovitch, and V. P. Yakovlev, *JETP Lett* **31** (1980).
- [39] A. Neuzner, M. Körber, S. Dürr, G. Rempe, and S. Ritter, *Phys. Rev. A* **92**, 053842 (2015).
- [40] C. F. Ockeloen, A. F. Tauschinsky, R. J. C. Spreeuw, and S. Whitlock, *Phys. Rev. A* **82**, 061606 (2010).
- [41] D. A. Steck, “Rubidium 87 d line data,” online (2010).
- [42] N. Solmeyer, K. Zhu, and D. S. Weiss, *Review of Scientific Instruments* **82**, 6 (2011).
- [43] A. Steffen, W. Alt, M. Genske, D. Meschede, C. Robens, and A. Alberti, *Review of Scientific Instruments* **84**, 25 (2013).
- [44] K. Zhu, N. Solmeyer, C. Tang, and D. S. Weiss, *Phys. Rev. Lett.* **111**, 1 (2013).
- [45] D. Budker and M. Romalis, *Nature Physics* **3**, 227 (2007).
- [46] M. Koschorreck, M. Napolitano, B. Dubost, and M. W. Mitchell, *Applied Physics Letters* **98**, 074101 (2011).
- [47] I. Bloch, *Nature Physics* **1**, 23 (2005).
- [48] M. Bruderer, a. Klein, S. R. Clark, and D. Jaksch, *New Journal of Physics* **10**, 033015 (2008).
- [49] A. Klein and M. Fleischhauer, *Phys. Rev. A* **71**, 033605 (2005).
- [50] F. Grusdt, A. Shashi, D. Abanin, and E. Demler, *Phys. Rev. A* **90**, 1 (2014).